A New Drag Correlation from Fully Resolved Simulations of Flow Past Monodisperse Static Arrays of Spheres

Y. (Yali) Tang, E. A. J. F. (Frank) Peters, and J. A. M. (Hans) Kuipers
Multiphase Reactors Group, Dept. of Chemical Engineering and Chemistry, Eindhoven University of Technology,
5600 MB Eindhoven, The Netherlands

S. H. L. (Sebastian) Kriebitzsch
Institute of Fluid Dynamics, Helmholtz-Zentrum Dresden-Rossendorf e.V., Dresden, Germany

M. A. (Martin) van der Hoef
Faculty of Science and Technology, University of Twente, Enschede, The Netherlands

DOI 10.1002/aic.14645

Fully resolved simulations of flow past fixed assemblies of monodisperse spheres in face-centered-cubic array or random configurations, are performed using an iterative immersed boundary method. A methodology has been applied such that the computed gas–solid force is almost independent of the grid resolution. Simulations extend the previously similar studies to a wider range of solids volume fraction ($\phi \in [0.1, 0.6]$) and Reynolds number ($Re \in [50, 1000]$). A new drag correlation combining the existed drag correlations for low-Re flows and single-sphere flows is proposed, which fits the entire dataset with an average relative deviation of 4%. This correlation is so far the best possible expression for the drag force in monodisperse static arrays of spheres, and is the most accurate basis to introduce the particle mobility for dynamic gas–solid systems, such as in fluidized beds. © 2014 American Institute of Chemical Engineers *AIChE J*, 61: 688–698, 2015

Keywords: immersed boundary method, fully resolved simulations, drag correlation

Introduction

Flows involving solid particles are encountered in a variety of industrial processes, where the gas and solid phases need to be brought into intimate contact. More specifically, these flows exist in gas-fluidized beds that are frequently applied in the chemical, environmental, petrochemical, metallurgical, and energy industries in large-scale operations involving physical (coating, drying, and granulation) and chemical transformation.[1] Traditionally, the design of fluidized beds (or other gas–solid contacting devices) is based primarily on empiricism, due to the lack of understanding of the hydrodynamics and the absence of quantitative prediction tools. To improve on this state-of-the-art, development and validation of computational models based on first principles is rapidly gaining attention to meet the needs for efficient future design, safe operation, and optimal control of fluidized beds. The prediction of dense gas–solid flows in engineering scale equipments can, in practice, only be achieved with continuum models. During the past decades, simulations based on either the Euler–Euler (two-fluid model[2]) or Euler–Lagrange (discrete element method DEM[3]) model have contributed to enhance our understanding of complex particulate flows. In these models, the flow between the particles is not resolved. Thus, the fluid-particle interactions are taken into account via effective transfer coefficients described by closure models. The accuracy of these closures determines the reliability of the results, hence the predictive capability of these models. This leads to an essential requirement on developing accurate closures accounting for those unresolved interactions.

One of the key inputs for numerical models of large-scale two-phase flows, such as in fluidized beds, is the closure for the momentum exchange between the particles and the gas. This is referred to as the drag law or drag correlation. In the past years, many closures for drag law have been proposed from theoretical, experimental, and computational studies. Closures from theoretical studies[4–6] are limited to small solids volume fractions (ϕ) and/or low Reynolds number (Re). For $\mathrm{Re} > 1$ and $\phi > 0.1$, there are a large number of empirical correlations, which are obtained from analysis of experimental data.[7,8] Crucial is that (1) the parameters in these correlations have been obtained empirically for idealized conditions, and do not apply for all situations that may occur in gas–solid systems; and (2) these experimental data only provide indirect information on the drag force through measurement of either the pressure drop or the terminal velocity of sedimenting particles. By contrast, direct numerical simulations (DNS, also called fully resolved simulations) have become a promising alternative tool, in which the interphase exchange is not

---

Correspondence concerning this article should be addressed to E. A. J. F. Peters at E.A.J.F.Peters@tue.nl.

modeled via empirical assumptions but follows from boundary conditions at the surface of the particles. The advantage is that not only the force can be "measured" directly, but also arbitrary material and flow conditions can be defined and perfectly controlled in simulations, which is not the case in experiments. DNS models can hereby provide the insight and data to formulate improved correlations for large-scale predictive models. A few drag correlations have been proposed on the basis of DNS results, covering a wide range of Re and ϕ (using Lattice-Boltzmann Method (LBM)[9–11] or Immersed Boundary Method (IBM)[12]). Most of the currently available closures were obtained for monodisperse systems of spherical particles, considering the average ϕ and mean Re. Importantly, they are considered as the basis to introduce more complexity in fluidized bed studies. For instance, the models for polydisperse suspensions[11,13,14] rest upon a drag law for an equivalent monodisperse suspension, by modification accounting for the polydispersity. Besides, a common approach in the so far reported studies of nonsphericity effect on fluidization and sedimentation[15–17] is to introduce the particles' sphericity into a drag correlation derived from spherical particles. Therefore, an accurate drag correlation for monodisperse systems of spheres is essential to improve the predictive capabilities of computational fluid dynamics (CFD) models for dense gas–solid flows.

As mentioned before, DNS provides an unprecedented capability to explore the fundamental mechanisms in gas–solid flows, for which most experimental and theoretical analysis are so far very limited. It has also been demonstrated that the incorporation of some DNS techniques into coupled DEM-CFD[18–20] can enhance the capacity of the conventional CFD model, on handling large objects or arbitrary shaped boundaries in problems such as gas fluidization with immersed tubes or dense solids with large size difference. In the past decades, several methods have been developed for DNS of gas–solid flows, such as the overset grid methods,[21] the Arbitrary Lagrangian–Eulerian Method,[22] PHYSALIS,[23] the LBM, and the IBM, and so on. We briefly discuss the LBM and IBM later, because of their relevance for the results reported in this article.

The LBM can be viewed as a special discretization of the Boltzmann equation on a lattice to mimic gas collisions. Hydrodynamic behavior emerges on longer length scales as a consequence of the momentum conversation of the collisions. The fluid-particle interactions are modeled using the so-called bounce back collision rules for the fluid. This method has been extensively used to study particle laden flows. It is particularly suitable when multiple moving objects are considered.[24] Although a calibration of the particle diameter is always required, LBM has been considered an outstanding method to investigate the drag law by detailed simulations of gas–solid flows. Ladd[25,26] first computed the drag force on particles in monodispersed suspensions of spheres using this method. Based on such LBM simulations for low-Reynolds-number flows, a drag correlation was derived by Hill et al.[9,27] Later on, the simulations were extended to monodisperse and bidisperse random arrays of spheres at moderate Reynolds number by van der Hoef et al.[13] and Beetstra et al.[11] In addition, studies have been reported on the clusters' effect on the drag force using this method.[28–30] For a recent overview on LBM for particulate flows, see Aidun and Clausen.[31]

The IBM is another widely used approach to model fluid-structure interactions. It was originally introduced by Peskin[32] for flows around flexible membranes, especially the flow in the human heart. The major advantage of IBM[33,34] is the efficient implementation of the no-slip condition for stationary and moving bodies with complex geometries. Specifically, the continuous phase is resolved by solving the Navier–Stokes (NS) equations on a fixed and typically structured Eulerian grid. The interaction between the phases is taken into account by adding a body force to the momentum equations, such that a no-slip boundary condition is fulfilled on the surface of the solid particles. Based on the traditional IBM concept, a direct-forcing immersed boundary (IB) approach was later on introduced,[35,36] in which the body force is computed from the discretized transport equations, accounting for the boundary conditions at the (Lagrangian) marker points distributed over the surface of the particles. This approach was further improved by Uhlmann,[37] and became the "so-called" Uhlmann method. In this method, a regularized delta function is used to distribute the force density from the Lagrangian point positions to the Eulerian grid points. Since then, the Uhlman method has been applied and proven suitable to problems such as flows over stationary and oscillating spheres/cylinders, sedimentation of discs and spheres, and so forth.[1,38–40] One of the downsides of using such a delta function is that the force density is distributed in a diffusive manner to a volume that is slightly larger than the solid particle size. As a result, the flow "feels" a bigger particle and the calculated interfacial transport mechanisms might not be completely correct. Many strategies have been proposed to overcome this issue. For instance, one idea is to retract the marker points slightly inward to the interior of the particles to yield the correct particle size.[41–43] We developed a methodology to obtain the effective retraction distance regarding to this approach.[44] Another approach proposed by Garg et al.[45] is to apply the force density only to the nodes located interior of a particle. Using this method, Tenneti et al.[12] calculated the drag force in dense arrays of spheres and obtained a drag correlation. Besides, Deen et al.[1] reported a method in which the treatment of the boundary conditions on particle surfaces is imposed by an interpolation method.

DNS models have largely contributed to the development of the fluid-particle momentum exchange closure, both by LBM and IBM as well. Such correlations are crucial for a correct understanding and quantitative description of the fluid-solid hydrodynamics. However, the studied parameter spaces do not cover all the situations encountered in gas–solid systems. To improve this, we carry out this work, aiming to derive a drag correlation for a wide range of Reynolds numbers and solids volume fractions, by DNS simulations using an iterative IBM. We have developed a methodology to obtain highly accurate (essentially grid-independent) results for the gas–solid force from IBM simulations at low computational cost. With this methodology, simulations are performed for the flow past fixed random arrays of monodisperse spheres, considering Re from 50 to 1000 and ϕ from 0.1 to 0.6. Besides, we utilize the existing drag correlations for low Re and small ϕ flows, which are not studied in our simulations. On the basis of all these results, a new correlation is developed, which describes the general drag law for the monodisperse static particulate flows.

This article is organized as the following: we first describe the drag correlations for monodisperse systems in literature; then, the iterative IB method and the modeling methodology is briefly introduced; subsequently, we report the simulation results of both face-centered-cubic (FCC) array and random configurations, based on which a new drag correlation is proposed; this is followed by the conclusions as well as discussions on the future work.

Description of Drag Law for Monodisperse Systems

Before presenting the literature drag correlations, it is essential to make clear how the drag force is defined. When a fluid percolates through assemblies of particles, each particle experiences two forces from the fluid, namely a buoyancy-type force $\mathbf{F}_b$ due to the average pressure gradient and a force $\mathbf{F}_d$ resulting from the local frictional losses. The sum of these two forces is the total force $\mathbf{F}_{g\to s}$ that the fluid exerts on a solid particle. The reaction force from the particles on the fluid manifests itself in a pressure drop. The forces are related to the pressure drop over the system as follow

$$-\nabla P=\frac{N_p}{V_{\text{sys}}}\mathbf{F}_{g\to s}=\frac{N_p}{V_{\text{sys}}}(\mathbf{F}_d+\mathbf{F}_b)=\frac{N_p}{V_{\text{sys}}}(\mathbf{F}_d-V_p\nabla P) \quad (1)$$

where N_p is the number of particles, V_{sys} the total system volume, and V_p the volume of a single particle. Equation 1 can be written as

$$-\nabla P=\frac{\phi}{1-\phi}\frac{\mathbf{F}_d}{V_p} \quad (2)$$

From Eqs. 1 and 2, it follows that

$$\mathbf{F}_{g\to s}=\frac{1}{1-\phi}\mathbf{F}_d \quad (3)$$

In literature both forces, the total gas–solid force[4,27] and the local frictional force,[13,46] are sometimes referred to as the drag force. As can be seen from Eq. 3, these two definitions of drag force[13] differ by a factor of $(1-\phi)$. To be clear, we report the friction-caused force as the drag force throughout this article, by a dimensionless force that is defined by normalizing the drag force $\mathbf{F}_d$ with the Stokes solution as $F_d=\mathbf{F}_d/(3\pi\mu d_p\mathbf{U})$, with $\mathbf{U}$ the superficial velocity. Note that the IBM simulation program calculates the force exerted on individual particles, which refers to $\mathbf{F}_{g\to s}$ in above equations. This force is converted to the drag force according to Eq. 3.

A detailed overview of drag force relations for monodisperse systems was given by Beetstra et al.[11] We now briefly describe the mostly applied drag correlations in literature. Correlations for the drag force of flow past static monodisperse arrays are usually of the form

$$F_d(\phi,\text{Re})=F_d(\phi,0)+\alpha\text{Re} \quad (4)$$

It is based on the drag force in the limit of Stokes flow $F_d(\phi,0)$, to which a term linear in Re is added accounting for the inertial effects.

For the functional form of $F_d(\phi,0)$ and α, the following expressions were suggested in the 1920s:

$$F_d(\phi,0)=\frac{a\phi}{18(1-\phi)^2},\ \alpha(\phi)=\frac{b}{18(1-\phi)^2} \quad (5)$$

Ergun[7] obtained the values of $a = 150$ and $b = 1.75$ on the basis of data for the pressure drop over packed beds of various materials from a large number of experiments. The combination of Eqs. 4 and 5 with these values of a and b is known as the Ergun equation, which is one of the most widely used correlations in engineering. Later on, more accurate experimental and simulation data were obtained for the drag force. It was then concluded that for dense fixed beds at low Reynolds numbers, Eq. 5 for $F_d(\phi,0)$ becomes more accurate with $a = 180$, which corresponds to Carman[6] equation. Finally, van der Hoef et al.[13] proposed the best fit (Eq. 6) to all simulation data for arbitrary solids volume fraction, which is a simple modification of the Carman equation

$$F_d(\phi,0)=\frac{180\phi}{18(1-\phi)^2}+(1-\phi)^2(1+1.5\sqrt{\phi}) \quad (6)$$

Conversely, the coefficient term α was later on found to be dependent on not only the solids volume fraction as in Eq. 5, but also the Reynolds number. Hill, Koch, and Ladd[9] carried out LBM simulations for intermediate-Re flows ($40<\text{Re}<120$), and proposed the following expression (referred as HKL) for an extended Re range

$$\alpha(\phi)=0.03365(1-\phi)+0.106\phi(1-\phi)+\frac{0.0116}{(1-\phi)^4}+\frac{\delta F}{\text{Re}} \quad (7)$$

where the term $\delta F/\text{Re}$ was added by Beetstra et al.[11] for a better prediction at $\text{Re}<200$, with a rough estimate for δF according to the original data

$$\delta F=\frac{6\phi-10\phi^2}{(1-\phi)^2} \quad (8)$$

Note that the drag relations proposed in Hill et al.[9] do not cover the full range of solids volume fraction or Reynolds number encountered in fluidized beds. To this end, Benyahia et al.[47] modified the HKL correlation to some blended functions that are continuous with respect to Re and ϕ.

Furthermore, extensive LBM simulations were performed by Beetstra et al.[11] for Reynolds number up to 1000. On the basis of their simulation data, a more complex functional form (referred as BVK) was proposed, instead of a linear scaling with Re assumed by the Ergun-type correlation

$$\alpha(\phi,\text{Re})=\frac{0.413}{24(1-\phi)^2}\times\left[\frac{(1-\phi)^{-1}+3\phi(1-\phi)+8.4\text{Re}^{-0.343}}{1+10^{3\phi}\text{Re}^{-(1+4\phi)/2}}\right] \quad (9)$$

Another widely used correlation in engineering (usually combined with Ergun equation) is Wen and Yu equation, which is of the form

$$F_d(\phi,\text{Re})=F_d(0,\text{Re})(1-\phi)^{-\beta} \quad (10)$$

where $F_d(0,\text{Re})$ is the expression for the drag force acting on a single particle, and $\beta=3.7$. However, Felice[46] found that β is actually independent of other system variables except for the Reynolds number. An expression of β was proposed

$$\beta=3.7-0.65\exp\left\{\frac{-(1.5-\log\text{Re})^2}{2}\right\} \quad (11)$$

Recently, Tenneti et al.[12] proposed a correlation of the average fluid-particle force, based on the DNS results for Re ≤ 300. The correlation is converted to the function of drag force as following (referred as TGS)

$$F_d(\phi,\mathrm{Re}) = \frac{F_d(0,\mathrm{Re})}{(1-\phi)^2} + \frac{5.81\phi}{(1-\phi)^2} + 0.48\frac{\phi^{1/3}}{(1-\phi)^3} + (1-\phi)\phi^3\mathrm{Re}\left[0.95 + \frac{0.61\phi^3}{(1-\phi)^2}\right] \tag{12}$$

in which, the single sphere drag correlation proposed by Schiller and Naumann[48] is used

$$F_d(0,\mathrm{Re}) = \begin{cases} 1+0.15\,\mathrm{Re}^{0.687} & \mathrm{Re} < 1000 \\ \dfrac{0.44}{24}\,\mathrm{Re} & \mathrm{Re} > 1000 \end{cases} \tag{13}$$

Method and Model

An iterative IBM is adopted in this work, which basically follows the Uhlmann method. Implementation details can be found in Kriebitzsch,[40] where extensive standard validations are given, such as the hydrodynamic force in low-Re flows past single sphere, regular and random arrays of spheres, as well as the interaction force between two-approaching spheres. We now give a brief description of this method below.

Numerical method

We model a system of static rigid spheres immersed in the flow of an incompressible Newtonian fluid. All physical properties are considered to be constant. The numerical model consists of the solution to the gas phase equations, the particle motion, and the gas–solid coupling.

The gas phase is governed by the NS equations, which are solved on a fixed and structured Eulerian grid with its grid size h much smaller than the particle diameter d_p. These equations are solved using state-of-the-art CFD methods, where second-order schemes are used for space and time discretization of the momentum equations, in which the convective, viscous, and pressure terms are treated in an explicit, semi-implicit, and implicit manner, respectively. For the solid phase, each particle is represented by a set of marker points that are specified in terms of a spherical diameter d_m. Traditionally, the marker points are uniformly distributed over the particle's surface, which means $d_m = d_p$. The motion (if there is) of particle i follows Newton's second law, from which the translational $\mathbf{v}_i$ and rotational $\mathbf{w}_i$ velocities are updated every CFD time step

$$m_{p,i}\frac{d}{dt}\mathbf{v}_i = (\rho_{p,i}-\rho_g)V_{p,i}\mathbf{g} + \mathbf{F}_{g\to s,i} + \sum_{j\neq i}\mathbf{F}_{c,j\to i} \tag{14}$$

$$\Theta_{p,i}\frac{d\mathbf{w}_i}{dt} = \mathbf{T}_{g\to s,i} + \sum_{j\neq i}\mathbf{T}_{c,j\to i} \tag{15}$$

with $m_{p,i}, \rho_{p,i}, V_{p,i}$ the mass, density, and volume of the particle i, respectively. The terms on the right-hand side of Eq. 14 are the gravity reduced by buoyancy, the hydrodynamic gas–solid force $\mathbf{F}_{g\to s,i}$, and the total collision force $\mathbf{F}_{c,j\to i}$ with other particles or the wall. While, for Eq. 15 they are the gas-particle torque $\mathbf{T}_{g\to s,i}$ and the total collisional torque. The particle–particle or particle-wall collisions are modeled by a hard-sphere method,[49] in which the particles interact via binary, instantaneous collisions. In addition, the moment of inertia for spheres is equal to $\Theta_{p,i} = (1/10)m_{p,i}d_{p,i}^2$. The hydrodynamic interactions the gas exerts on a particle are obtained by

$$\mathbf{F}_{g\to s,i} = -\oint_{\Gamma_i}(P\mathbf{n} + \mathbf{S}\cdot\mathbf{n})d\sigma \tag{16}$$

$$\mathbf{T}_{g\to s,i} = -\oint_{\Gamma_i}((\mathbf{x}-\mathbf{r}_i)\times(\mathbf{S}\cdot\mathbf{n}))d\sigma \tag{17}$$

where $\mathbf{x}-\mathbf{r}_i$ is the vector from the mass center $\mathbf{r}_i$ of particle i to a marker point x on its surface Γ_i; $\mathbf{S}$ represents the viscous stress tensor

$$\mathbf{S} = -\mu_g[\nabla\mathbf{u} + (\nabla\mathbf{u})^T] \tag{18}$$

Additionally, the gas–solid coupling is enforced by adding a force term to the NS equations of the fluid phase. This force term is computed at each marker point such that the no-slip condition is enforced on the surface of the particles, which means that the local velocity of the gas has to be equal to the velocity at that position at the particle surface. The sum of this force term from the marker points of one particle is equal to the total force that the particle applies to the fluid. A function is required to couple the data on the Lagrangian markers with the corresponding variables defined on the Eulerian grids, or to be more specific for the velocity interpolation and the force distribution between the marker points and the adjacent grid points. To this end, a regularized delta function suggested by Deen et al.[50] is employed, which is a cheap clipped fourth-order polynomial function with a finite support of three times the grid size. Besides, an additional iteration procedure is adopted to achieve a more accurate enforcement of the no-slip boundary condition in an efficient way. The numerical scheme of our iterative IBM is illustrated in Figure 1, with each step explained as follows.

1. First, the preliminary fluid velocity field $\hat{\mathbf{u}}^0$ is calculated, assuming no presence of particles. In Figure 1, we introduce: gas density ρ_g, gas velocity $\mathbf{u}$, modified pressure $P = p - \rho_g\mathbf{g}\cdot\mathbf{x}$, the stress tensor S, the convective term C, time step Δt; and the subscript n as the current time step.
2. Velocity interpolation from the surrounding grid points $\mathbf{x}_{i,j,k}$ to the position $\mathbf{X}_m$ of marker point m, via the regularized delta function $D(x-X)$. The subscript n_s represents the iteration number, whereas h is the grid size.
3. IB force $\mathbf{F}^{\mathrm{IB}}$ calculation at each marker point, based on the slip velocity between the local fluid velocity $\mathbf{U}_m$ and the particle velocity $\mathbf{v}_m$.
4. Distribution of the force density at the marker point over the surrounding grid points, with the volume of each marker point ΔV_m.
5. Calculation of intermediate velocity field $\hat{\mathbf{u}}$, with the presence of particles considered by adding the IB force density. $\mathbf{L}$ is the operator of the spatial discretization of the Laplacian ∇, and $\mathbf{I}$ is the unit tensor.
6. Determine if the no-slip boundary condition is fulfilled up to the specific level of accuracy ε, or the maximum iteration number $n_{s,\max}$ is reached. If true, the computation goes on to the next step; otherwise, it goes back to the iteration loop.
7. Solve Poisson equation for pressure correction.
8. Update to the new velocity field $\mathbf{u}^{n+1}$ and pressure field P^{n+1}.

Corrections for grid-size effects

For this type of IBM, the results have been shown to possess a strong grid dependence, which means that a high

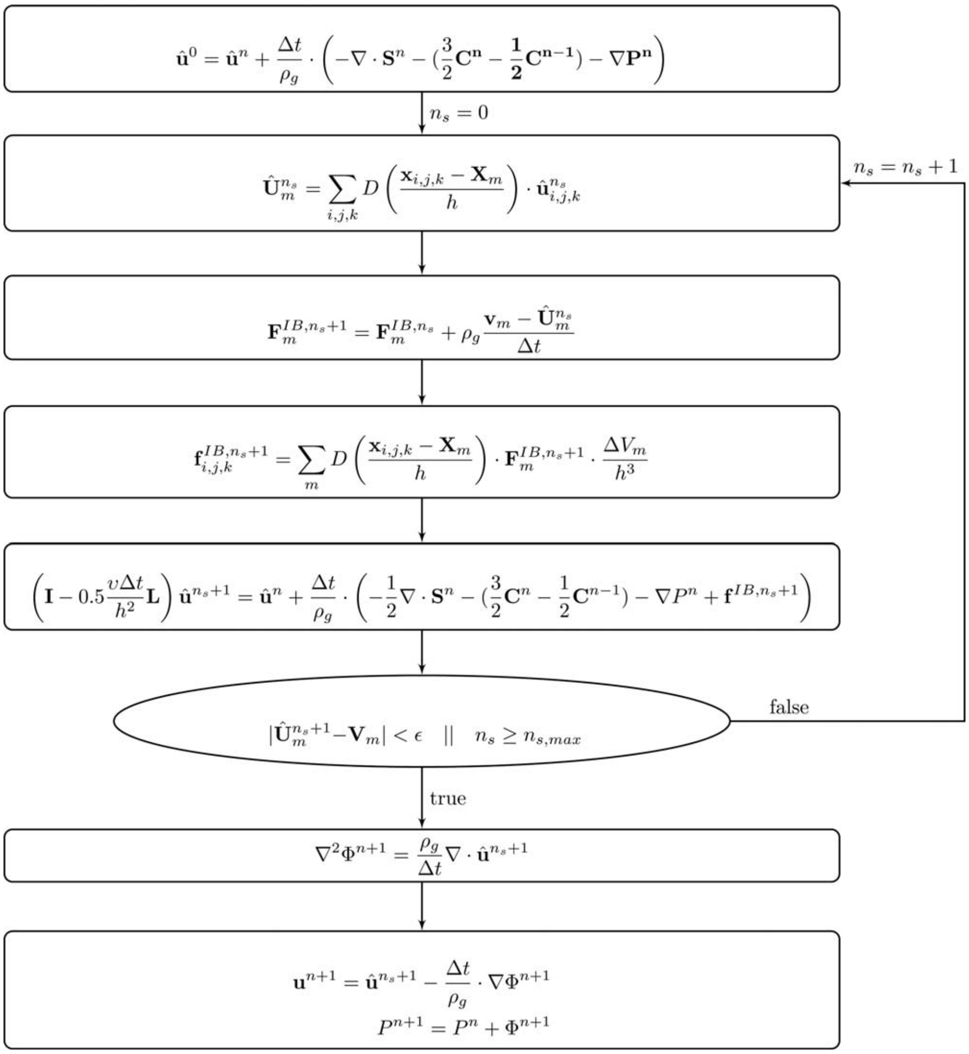

Figure 1. Calculation of the velocity and the force term during one time step in the iterative IBM.

resolution (particle diameter/grid size ratio) is usually required especially for problems involving high solids volume fraction and/or high Reynolds number flows.[33,34,51] In fact, even for low Reynolds numbers, Kriebitzsch[40] observed a departure of the finite-resolution simulation results from the exact values for the drag force on a particle in regular arrays given by Hasimoto.[4] It was also indicated that this departure can be eliminated by modifying the diameter d_m for the marker points, which exactly follows the concept of "effective hydrodynamic diameter" proposed by Ladd[26] for the lattice Boltzmann method. This modified diameter was chosen such that the simulation data at a finite grid resolution matches the theoretical solution for the drag force. However, the theoretical/exact solution for the drag force is limited to very low Reynolds number and small solids volume fraction. Therefore, for high-Re flows, which are the target problems studied in this work, we have developed a methodology to deal with the issue of grid-size effects. Details and verifications have been reported in Tang et al.,[44] while only a brief outline of this methodology is given here.

First, IBM simulations are performed at different resolutions to calculate the gas–solid interaction force of flows past FCC arrays of spheres at certain values of ϕ and Re. Such a simulation can be carried out at a very high resolution due to the low computational cost as only four particles are needed for the adopted periodic boundary conditions. Subsequently, a "resolution-free" drag force F_d^{FCC} is obtained by extrapolating these simulation data to an infinite resolution. By doing this for various solids volume fractions, one can formulate a function of F_d^{FCC} versus ϕ at a certain Re. This function is then used to evaluate how much the value of ϕ should be modified such that the data for a particular resolution exactly matches F_d^{FCC}. The modification of ϕ can be easily converted to the calibration of diameter d_m for the marker points' distribution. Finally, prediction of the interaction force in random arrays of spheres is carried out with simulations at a low resolution, with the d_m modified correspondingly.

IBM Simulations of Flow Past Static Arrays

The methodology described earlier has been applied in our IBM simulations to predict the drag force in gas flows past fixed random arrays of monodisperse spheres. Different combinations of Reynolds number (Re∈[50, 1000]) and solids volume fraction (ϕ ∈[0.1, 0.6]) have been studied.

Simulation set-up

The problem considered in this work is fluid flow through spherical particles arranged in regular or random arrays in a periodic 3-D box, seen in Figure 2 as an example of the

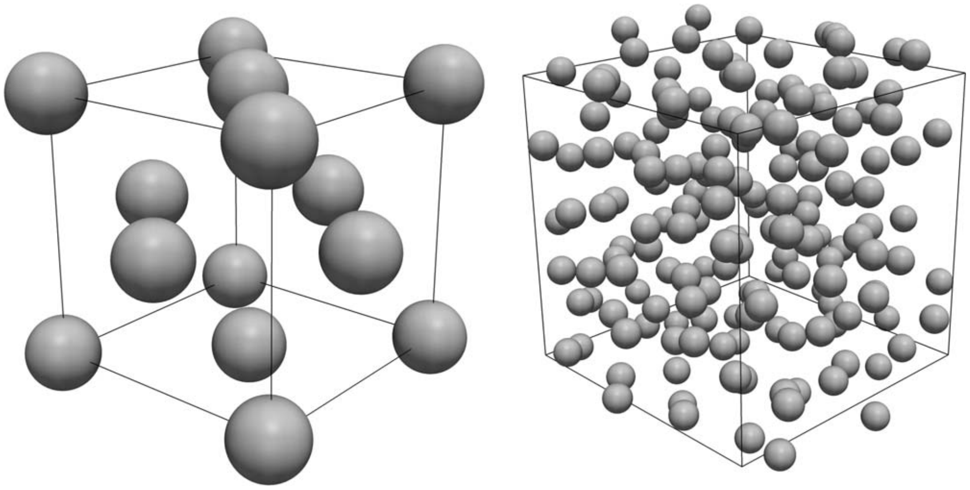

Figure 2. Particle configuration at $\phi = 0.4$ of FCC (left) and random (right) arrays in a periodic 3-D box.

The particles are scaled by 50% for visualization.

particle configurations. In the simulations, all the particles are given the same constant velocity v so that the entire array moves as a static configuration through the domain. A uniform body force is applied to the fluid phase, such that the superficial velocity U of the fluid relative to the uniformly moving particles is equal to the negative particle velocity ($-v$), resulting in the Reynolds number $\mathrm{Re}=\rho_g d_p |v|/\mu_g$. The physical properties of the fluid and the solids are listed in Table 1. The computational domain size is set by the solids volume fraction ϕ, the particle diameter d_p, and the number of particles N_p.

For the simulations of FCC arrays, only a unit cell of four particles is modeled, as periodic boundary conditions are employed. The resolutions that for use range from 12 up to 64 cells per particle diameter (80 for Re = {800, 1000}). The maximum iteration number is set to $n_{s,\max}=5$, which is sufficient for accurate enforcement of the no-slip condition. Simulations of periodic random arrays are carried out with $N_p = 108$ spheres positioned in 10–20 different configurations. The maximum iteration number is then set to $n_{s,\max}=3$, which is high enough to achieve the required accuracy while avoiding unnecessary increase in computational costs.[43] The grid resolution is chosen as $d_p/h \approx 16$ for Re = {50, 100} and $d_p/h \approx 12$ for Re = {200, 500, 800, 1000}, with individual modified d_m according to different combinations of (Re, $d_p/h, \phi$).[44] The random configurations are generated as follows. For $\phi \leq 0.45$, a standard hard sphere Monte-Carlo (MC) method[52] is applied: all the particles are initially placed in an ordered FCC configuration; then each particle is randomly moved, with the displacement accepted only if no overlap occurred at the new position with any other particle. Unfortunately, such a standard MC method is not suited to provide sufficient randomization for highly dense packings.[53] Therefore, the random configurations at $\phi > 0.45$ are created in this work using an event-driven method combined with particle swelling procedure,[54] which drastically improves the randomness as being seen from the radial pair distribution function that we have examined.

Table 1. Data Used for the Simulations of Static Sphere Arrays

Parameter	Value
Particle number N_p	FCC: 4, random: 108
Particle diameter d_p	1.6×10^{-3} m
Particle density ρ_p	500 kg/m^3
Fluid density ρ_g	1.0 kg/m^3
Fluid viscosity μ_g	1×10^{-5} kg/(m s)
Solids fraction ϕ	0.1, 0.15, 0.2, 0.25, 0.3, 0.35, 0.4, 0.45, 0.5, 0.55, 0.6
Reynolds number Re	50, 100, 200, 500, 800, 1000

Simulation results

In Figure 3, we present the obtained drag force F_d^{FCC} (symbols) for FCC arrays as a function of ϕ at different Reynolds numbers, together with the corresponding fit (lines) formulated in Eq. 19 with parameter values listed in Table 2. A very good agreement between the fit and data is achieved and shown in this figure. We stress that this function has no physical origin but is chosen such as to provide the best possible fit to each set of data at specific Reynolds number.

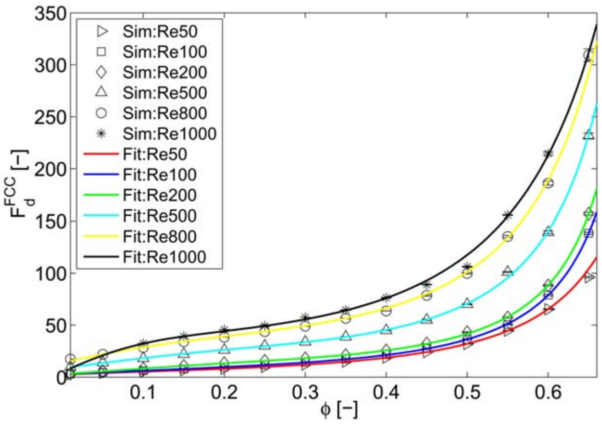

Figure 3. The dimensionless drag force in FCC arrays of spheres at different Reynolds numbers (see legend).

The symbols represent the obtained data and the lines are from Eq. 19. [Color figure can be viewed in the online issue, which is available at wileyonlinelibrary.com.]

Table 2. Parameters in Eq. 19 for Different Reynolds Numbers

Re	a	b	c	d	e
50	0.4765	−0.2694	−0.6410	0.9255	−0.5904
100	0.2829	1.6162	−3.3701	2.4318	−1.1539
200	0.3619	0.8975	−2.783	2.645	−1.332
500	0.01395	1.546	−2.618	1.714	−0.7608
800	0.0425	0.5563	−1.055	0.797	−0.3879
1000	0.4309	−2.958	3.385	−0.9059	0.04115

$$F_d^{\mathrm{FCC}}=\frac{1}{(1-\phi)^2}\cdot\frac{1}{a+b\phi^{1/3}+c\phi^{1/2}+d\phi+e\phi^2},\quad \text{specified Re} \tag{19}$$

For the completeness, we have also fitted those results of drag force in FCC array to a general function of Re and ϕ as Eq. 20, with an average relative deviation of 6.0%. This correlation is slightly less accurate than expression Eq. 19, but has the advantage of providing an estimate of F_d^{FCC} at arbitrary Re (≤ 1000) and ϕ. To our knowledge, this type of expression for the drag force in FCC array, which is based on DNS simulation results over a wide range of Reynolds number (Re ≤ 1000), has not been reported in literature before.

$$20F_d^{\mathrm{FCC}}(\phi,\mathrm{Re})=\frac{10\phi}{(1-\phi)^2}+(1-\phi)^2(1+1.5\sqrt{\phi})+\left[0.043\phi(1+\phi)+0.028(1-\phi)+\frac{0.0545\mathrm{Re}^{-0.343}-0.00257}{(1-\phi)^4}\right]\mathrm{Re} \tag{20}$$

As indicated earlier, in this work, we use the highly accurate data of drag force obtained for FCC array to calibrate the diameter d_m. This modified d_m is used for the distribution of the marker points, which allows for a more accurate evaluation of the gas–solid interaction force and an improved flow field computed from IBM simulations while using a relatively coarse computational grid.[44] It is calculated from Eq. 19 along with parameter values in Table 2 by an iterative procedure using Newton's method, together with the simulation force data for FCC arrays at different combination of (Re, $\phi, d_p/h$). The results of modified d_m are found to be dependent on Reynolds number, grid resolution, and solids volume fraction as well. These results are then applied for the simulations of random arrays, with which the prediction of the drag force can be implemented at a relatively low resolution.

Finally, the results of dimensionless drag force F_d for random arrays are given in Table 3 for different Reynolds numbers and solids volume fractions. F_d is the average over 10–20 different random configurations, whereas ΔF is the standard deviation.

A new drag correlation

We have computed the average gas–solid drag force in random arrays for several values of Re and over a wide range of ϕ, with the data reported in Table 3. To acquire a single drag relation for the entire parameter space of Re and ϕ, we also included results from existing relations for low-Re flows and single-sphere flows. On basis of all these data, we develop a drag correlation with the form of Eq. 4, which gives a good fit with an average relative deviation of $|F_d^{\mathrm{sim}}-F_d|/F_d^{\mathrm{sim}}=4\%$:

$$F_d(\phi,\mathrm{Re})=\frac{10\phi}{(1-\phi)^2}+(1-\phi)^2(1+1.5\sqrt{\phi})+\left[0.11\phi(1+\phi)-\frac{0.00456}{(1-\phi)^4}+\left(0.169(1-\phi)+\frac{0.0644}{(1-\phi)^4}\right)\mathrm{Re}^{-0.343}\right]\mathrm{Re} \tag{21}$$

Note that this correlation has been combined with Eq. 6, which has been considered the most accurate description for the drag force in low-Re flows. Furthermore, the drag on an isolated sphere resulting from the correlations (Eq. 13) proposed by Schiller and Naumann[48] is also taken into account, and shown in Figure 4 with symbols at $\phi=0$. In this figure, $F_d(\phi,\mathrm{Re})\cdot(1-\phi)^2$ calculated from Eq. 21 is shown by solid lines, together with the IBM data (symbols) from Table 3. We also include some existing drag correlations for

Table 3. Average Dimensionless Drag Force in Flows Through Random Arrays

Re	ϕ	0.1	0.15	0.2	0.25	0.3	0.35	0.4	0.45	0.5	0.55	0.6
50	F_d	5.7202	7.1808	8.8008	11.143	13.067	17.033	21.402	27.139	35.261	47.462	67.920
	ΔF	0.1000	0.10426	0.1371	0.159	0.170	0.191	0.266	0.239	0.453	0.714	0.789
100	F_d	8.6390	10.124	12.288	14.869	18.206	22.169	27.512	34.368	46.144	65.304	87.868
	ΔF	0.2002	0.253	0.266	0.290	0.318	0.411	0.552	0.655	0.768	1.234	1.232
200	F_d	10.671	13.285	18.205	19.801	24.149	28.261	33.951	42.528	54.425	71.253	99.360
	ΔF	0.221	0.275	0.301	0.464	0.327	0.351	0.600	0.912	0.895	1.389	1.178
500	F_d	18.402	23.143	27.179	37.235	39.750	49.447	58.502	77.414	89.040	112.76	155.12
	ΔF	0.148	0.261	0.299	0.307	0.887	0.492	0.604	0.609	0.754	1.15	1.79
800	F_d	28.619	35.147	39.270	48.597	59.533	72.449	83.016	97.685	122.55	157.17	197.51
	ΔF	0.420	0.302	1.101	0.662	0.457	0.580	0.971	1.054	1.04	1.55	2.22
1000	F_d	31.633	39.196	45.516	62.684	68.719	82.245	102.70	111.42	140.22	172.19	208.50
	ΔF	0.389	0.480	0.383	0.595	0.480	1.010	1.27	1.20	1.12	1.62	2.23

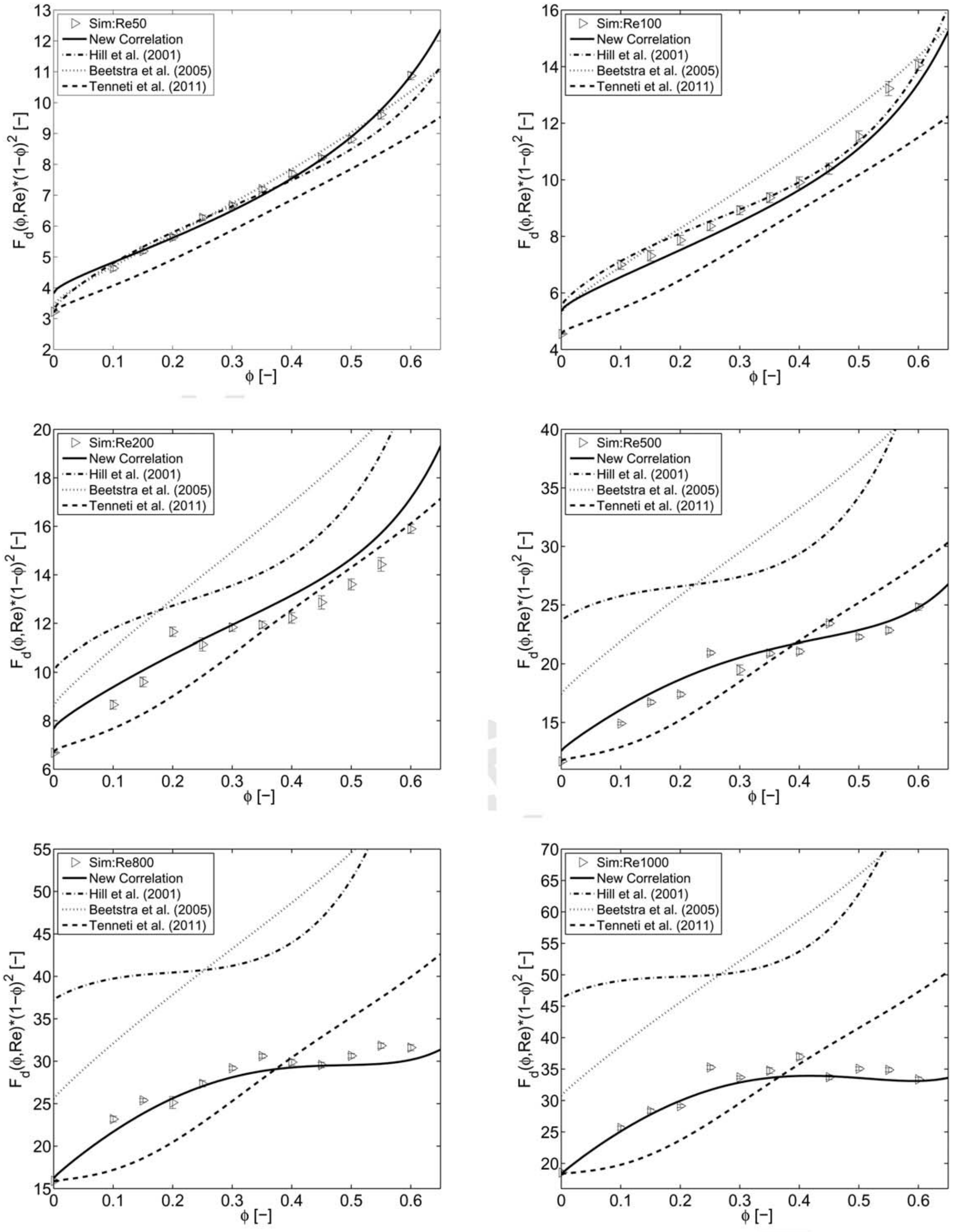

Figure 4. $F_d(\phi, \mathrm{Re}) \cdot (1-\phi)^2$ as a function of the solids volume fraction ϕ, for Reynolds number Re = {50, 100, 200, 500, 800, 1000} in sequence.

$F_d(\phi, \mathrm{Re})$ used in figures are: (symbols) the simulation data in Table 3 and the single-sphere drag correlation results (at $\phi \to 0$) with the error bars for the standard errors; (solid lines) Eq. 21; (dash-dot lines) the HKL; (dotted lines) the BVK; (dashed lines) the TGS.

comparison: HKL (dash-dot lines), BVK (dotted lines), and TGS (dashed lines). It can be seen that our new correlation provides quite a good fit to the data of IBM simulations.

In general, the HKL and the BVK correlations are in a reasonable agreement with the results at lower Reynolds number of 50 and 100, but markedly differ from those at higher Re. This observation is consistent with the results reported by Tenneti et al.,[12] who concluded that the HKL correlation was valid only up to Re = 100 and BVK correlation was with more than 30% difference from their simulation data up to Re = 300. In Figure 4, we see that the differences between HKL drag law and our new correlation increase with Reynolds number when Re beyond 100. However, as HKL drag law was extended from LBM simulation results of Re < 120, such discrepancy is not surprising.

Differences between the BVK and our IBM correlation increase significantly with increasing Reynolds number and are noticed more pronounced for larger solids volume fractions. In BVK, a constant resolution of 17.5 lattice units across a particle diameter was used for $\phi \leq 0.2$, and for higher solids volume fractions they obtained average results over two resolutions of 17.5 and 25.5 lattice units. As we know for denser packings, there are more narrow gaps between particles, which require higher resolution for DNS simulations. Therefore, using a constant resolution for a range of volume fractions from 0.2 up to 0.6, BVK drag law is under resolved and the grid size effects on the results are enhanced with increasing ϕ. This is consistent with our observation from Figure 4. Comparing to both HKL and BVK, our IBM simulations are consistently better resolved in terms of grid resolution effects, especially for high Reynolds numbers and dense packings. However, in Figure 4, there is another observation specially from the HKL correlation, that is, it can qualitatively capture the changing of $F_d(\phi, \mathrm{Re}) \cdot (1-\phi)^2$ with increasing ϕ, regardless of the Reynolds number. In fact, this observation became the rationale for adopting a similar functional form of $\alpha(\phi, \mathrm{Re})$ from the HKL correlation to our new correlation Eq. 21. Consequently, as is seen in Figure 4, our new correlation not only gives the best possible estimate of the data, but also describes the detailed dependency.

Besides, it is shown that the TGS correlation predicts drag forces in the same order of magnitude as our simulation data for most of the Reynolds numbers studied. However, it does not describe changing shape of $F_d(\phi, \mathrm{Re}) \cdot (1-\phi)^2$ with increasing ϕ, as the HKL correlation and Eq. 21 do. Based on their simulation results, TGS[12] correlation is a fitting function applying the drag force $F_{\mathrm{isol}}(\mathrm{Re})$ acting on an isolated sphere moving in an unbounded medium, for which they used the single sphere drag correlation proposed by Schiller and Naumann.[48] We can see from Figure 4 that the TGS meets all the data points at $\phi \rightarrow 0$, which represent the force values from single sphere drag laws. However, finding accurate estimation for $F_{\mathrm{isol}}(\mathrm{Re})$ or $F(0, \mathrm{Re})$ has challenged the scientific community for a large number of years. Our current knowledge is mainly based on experimental data as the correlation by Schiller and Naumann.[48] Numerical simulations of such systems challenge the computational cost due to the required unbounded domain. Conversely, the development of drag laws for Stokes flows $F(\phi, 0)$ is more mature from DNS. For instance, we apply the correlation proposed by van der Hoef et al.[13] that is a simple modification of the Carman[6] equation based on LBM simulations of low-Reynolds-number flow past spheres for an entire range of ϕ. As a starting point for deriving a defined drag correlation, taking $F_{\mathrm{isol}}(\mathrm{Re})$ as in TGS or $F(\phi, 0)$ as in our new correlation Eq. 21 might lead to such discrepancies in Figure 4 for predicting the drag force in general flow conditions. Finally, the current IBM simulations are better considered in terms of the number of particles ($N_p = 108$ vs. TGS: $N_p \leq 41$ for $\mathrm{Re} > 100$) as well as Reynolds numbers ($\mathrm{Re} \leq 1000$ vs. TGS: $\mathrm{Re} \leq 300$).

Conclusions

In this work, we computed the drag force in flow past static monodisperse arrays of spheres using an iterative IBM. A methodology that improves the accuracy of the computed gas–solid interaction force and the flow field is applied for simulations at relatively low resolutions.[44] A large number of simulations have been performed for Reynolds number ranging from 50 to 1000 and solids volume fraction from 0.1 up to 0.6, with the data reported in Table 3. In all the simulations, the diameter d_m for marker points' distribution is evaluated individually for the specific combination of (Re, $\phi, d_p/h$) in order to bring the IBM force results as close as possible to be grid-size independent. Besides, we have carefully created particle configurations with a high degree of randomness, especially for dense packings. Note that each random configuration considered in this work consists of 108 particles, which is a larger number in comparison to the similar type of simulations reported in literature.

Apart from the IBM data of the studied simulations, we also considered the drag force from existing correlations for low-Re flows and single-sphere flows. Finally, a new drag correlation Eq. 21 for monodisperse suspensions was developed, which covers an entire range of solids volume fractions and Reynolds numbers up to 1000. This expression has a quite simple form, but gives a good estimate for the effective drag force with an average relative deviation of 4% with respect to the basic data. It is then compared with some correlations in literature. It turns out that both HKL and BVK correlations agree well with the drag results for $\mathrm{Re} \leq 100$, but have a significant deviation at higher Reynolds numbers regardless of ϕ. Conversely, the TGS correlation gives force results that are fairly close to our simulation data. However, it does not describe the detailed change of the drag force with the solids volume fraction. In the previous section, we have analyzed the discrepancies between our new drag correlation and the other referred correlations. In Table 4, we would like to further compare the parameter space of the number of particles N_p, Re, ϕ, and grid resolution for the DNS simulations, based on which these drag correlations are proposed. It is clear that our current IBM simulations have considered a larger number of spheres than the others. The HKL and TGS correlations are extended from simulation results for $\mathrm{Re} < 120$ and $\mathrm{Re} \leq 300$, respectively. While, the simulations for the BVK correlations are not as highly resolved as the others using constant resolutions for the wide range of studied Re and ϕ. Moreover, the TGS correlation does not involve simulation results for very dense system ([0.5, 0.6] is a very important range for fluidized bed studies). In contrast, all of these parameters have been studied

Table 4. Comparison of the Studied Parameters (N_p, Re, ϕ, and Grid Resolution) for DNS Simulations of Different Drag Correlations

Correlation	N_p ($\mathrm{Re} > 100$)	Re	ϕ	Resolution
HKL	16	$40 < \mathrm{Re} < 120$	Up to 0.641	9.6–41.6
BVK	54	$20 < \mathrm{Re} < 1000$	6 values in [0.1, 0.6]	17.5, 25.5
TGS	≤ 41	$\mathrm{Re} \leq 300$	5 values in [0.1, 0.5]	20–60
Equation 21	108	$\mathrm{Re} \leq 1000$	11 values in [0.1, 0.6]	Evaluated d_m

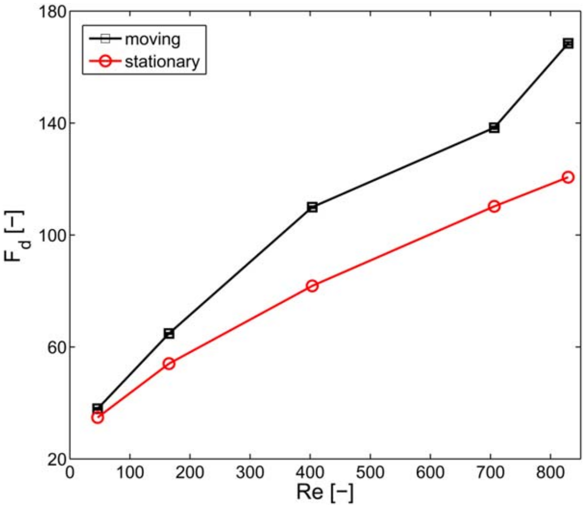

Figure 5. Dimensionless drag force in flow past sphere assemblies at solids volume fraction $\phi = 0.5$ as a function of Re based on the superficial velocity: stationary spheres vs. moving spheres.

[Color figure can be viewed in the online issue, which is available at wileyonlinelibrary.com.]

with a larger space in this work. Note that the d_m, which is used to correct for the resolution effect in this work, was evaluated on the basis of simulation results of FCC array with resolution up to 64 for low Re and 80 for high Re. We believe that at present Eq. 21 provides more accurate drag for flow past monodisperse static arrays of spheres for $\text{Re} \leq 1000$.

Discussions

So far, we have reported the simulation results of stationary particle assemblies and correspondingly proposed a new drag correlation. This correlation is considered so-far the best possible prediction of the drag force in static monodisperse arrays, but it does not capture the effect of particle mobility. In fact, none of the DNS-based correlations referred in this article has considered this effect. However, an increase of the dimensionless drag force with the particle mobility characterized by the granular temperature has been reported, for instance by Wylie et al.[55] and Kriebitzsch et al.[56] as well. For this reason, we performed IBM simulations of flows past freely moving spheres at solids volume fraction of 0.5 for different flow Reynolds numbers (based on the superficial velocity). The simulation setups are the same as for static random arrays reported in this article, except that the particles can freely move with respect to the grid. Elastic collisions between particles are taken into consideration in these simulations. We average the local solids volume fraction and the velocity over the computational domain and over a certain time period after a steady particle granular temperature is reached. Figure 5 compares the dimensionless drag force as a function of Re between stationary particles and moving particles. It is seen that the mean gas–solid drag force in systems with freely moving particles, such as fluidized beds, is higher than for the systems with the same porosity and superficial velocity but stationary particles. The relative deviation of F_d between stationary and moving particles in this system case is about 20% for Re of about 800. Clearly, one can conclude that accurate drag correlations for static monodisperse arrays of spheres are not *a priori* applicable to large-scale modeling of fluidized beds.

Conversely, the fixed bed approximation is still significant for the study of high Stokes number particles that are characteristic of the gas–solid flows, such as in fluidized beds. The study of static systems can give the insights for the dependence of the gas–solid interaction force on the mean flow Reynolds number and mean solids volume fraction, which also applies for the systems involving moving particles. The increase of the gas–solid force resulting from particles' motion can be subsequently described by introducing the particle granular temperature into the basic drag correlation for static systems. This indicates that a very accurate drag correlation for static systems (like Eq. 21) is not sufficient, but essential for understanding of gas–solid flows such as in fluidization systems.

Acknowledgment

The authors would like to thank the European Research Council for its financial support, under its Advanced Investigator Grant Scheme, contract number 247298 (Multiscale Flows).

Literature Cited

1. Deen NG, Kriebitzsch SHL, van der Hoef MA, Kuipers JAM. Direct numerical simulation of flow and heat transfer in dense fluid-particle systems. *Chem Eng Sci*. 2012;81:329–344.
2. Panneerselvam R, Savithri S, Surender GD. CFD simulation of hydrodynamics of gas-liquid-solid fluidised bed reactor. *Chem Eng Sci*. 2009;64(6):1119–1135.
3. Oevermann M, Gerber S, Behrendt F. Euler-Lagrange/DEM simulation of wood gasification in a bubbling fluidized bed reactor. *Particuology*. 2009;7(4):307–316.
4. Hasimoto H. On the periodic fundamental solutions of the Stokes equations and their application to viscous flow past a cubic array of spheres. *J Fluid Mech*. 1959;5(2):317–328.
5. Sangani AS, Acrivos A. Slow flow through a periodic array of spheres. *Int J Multiphase Flow*. 1982;8(4):343–360.
6. Carman PC. Fluid flow through granular beds. *Trans Inst Chem Eng*. 1937;15:150–166.
7. Ergun S. Fluid flow through packed columns. *Chem Eng Prog*. 1952;48:89–94.
8. Wen CY, Yu YH. Mechanics of fluidization. *Chem Eng Prog Symp Ser*. 1962;62:100–111.
9. Hill RJ, Koch DL, Ladd AJC. Moderate-Reynolds-number flows in ordered and random arrays of spheres. *J Fluid Mech*. 2001;448:243–278.
10. Kandhai D, Derksen JJ, Van den Akker HEA. Interphase drag coefficients in gassolid flows. *AIChE J*. 2003;49(4):1060–1065.
11. Beetstra R, van der Hoef MA, Kuipers JAM. Drag force of intermediate Reynolds number flow past mono- and bidisperse arrays of spheres. *AIChE J*. 2007;53(2):489–501.
12. Tenneti S, Garg R, Subramaniam S. Drag law for monodisperse gas-solid systems using particle-resolved direct numerical simulation of flow past fixed assemblies of spheres. *Int J Multiphase Flow*. 2011;37(9):1072–1092.
13. van der Hoef MA, Beetstra R, Kuipers JAM. Lattice-Boltzmann simulations of low-Reynolds-number flow past mono- and bidisperse arrays of spheres: results for the permeability and drag force. *J Fluid Mech*. 2005;528:233–254.
14. Holloway W, Yin X, Sundaresan S. Fluid-particle drag in inertial polydisperse gas-solid suspensions. *AIChE J*. 2010;56(8):1995–2004.
15. Richardson JF, Zaki WN. Sedimentation and fluidisition: part I. *Trans Inst Chem Eng*. 1954;32:S82–S100.
16. Fonseca F, Herrmann HJ. Sedimentation of oblate ellipsoids at low and moderate Reynolds numbers. *Physica A*. 2004;342(34):447–461.
17. Shardt O, Derksen JJ. Direct simulations of dense suspensions of non-spherical particles. *Int J Multiphase Flow*. 2012;47:25–36.

18. Guo Y, Wu CY, Thornton C. Modeling gas-particle two-phase flows with complex and moving boundaries using DEM-CFD with an immersed boundary method. *AIChE J*. 2013;59(4):1075–1087.
19. Dietiker JF, Li T, Garg R, Shahnam M. Cartesian grid simulations of gas–solids flow systems with complex geometry. *Powder Technol*. 2013;235:696–705.
20. Tsuji T, Higashida K, Okuyama Y, Tanaka T. Fictitious particle method: a numerical model for flows including dense solids with large size difference. *AIChE J*. 2014;60(5):1606–1620.
21. Burton TM, Eaton JK. Analysis of a fractional-step method on overset grids. *J Comput Phys*. 2002;177(2):336–364.
22. Hu H, Patankar NA, Zhu MY. Direct numerical simulations of fluid-solid systems using the arbitrary Lagrangian-Eulerian technique. *J Comput Phys*. 2001;169(2):427–462.
23. Zhang Z, Prosperetti A. A second-order method for three-dimensional particle simulation. *J Comput Phys*. 2005;210(1):292–324.
24. Ten Cate A, Nieuwstad CH, Derksen JJ, Van den Akker HEA. Particle imaging velocimetry experiments and lattice-Boltzmann simulations on a single sphere settling under gravity. *Phys Fluids*. 2002;14(11):4012–4025.
25. Ladd AJC. Numerical simulations of particulate suspensions via a discretized Boltzmann equation. Part 1. Theoretical foundation. *J Fluid Mech*. 1994;271:285–309.
26. Ladd AJC. Numerical simulations of particulate suspensions via a discretized Boltzmann equation. Part 2. Numerical results. *J Fluid Mech*. 1994;271:311–339.
27. Hill RJ, Koch DL, Ladd AJC. The first effects of fluid inertia on flows in ordered and random arrays of spheres. *J Fluid Mech*. 2001; 448:213–241.
28. Beetstra R. Drag force in random arrays of mono- and bidisperse spheres. Ph.D. Thesis. Enschede, The Netherlands: University of Twente, 2005.
29. Shah MT, Utikar RP, Tade MO, Evans GM, Pareek VK. Effect of a cluster on gas-solid drag frim lattice Boltzmann simulations. *Ninth International Conference on CFD in the Minerals and Process Industries*. CSIRO, Melbourne, Australia, 2012.
30. Ernst M, Dietzel M, Sommerfeld M. A lattice Boltzmann method for simulating transport and agglomeration of resolved particles. *Acta Mech*. 2013;224(10):2425–2449.
31. Aidun CK, Clausen JR. Lattice-Boltzmann method for complex flows. *Annu Rev Fluid Mech*. 2010;42(1):439–472.
32. Peskin CS. Numerical analysis of blood flow in the heart. *J Comput Phys*. 1977;25(3):220–252.
33. Peskin CS. The immersed boundary method. *Acta Numer*. 2002;11: 479–517.
34. Mittal R, Iaccarino G. Immersed boundary methods. *Annu Rev Fluid Mech*. 2005;37:239–261.
35. Mohd-Yusof J. Combined immersed-boundary/B-spline methods for simulations of flow in complex geometries. Ann Res Briefs, Center for Turbulence Research. 1997:317–327.
36. Fadlun EA, Verzicco R, Orlandi P, Mohd-Yusof J. Combined immersed-boundary finite-difference methods for three-dimensional complex flow simulations. *J Comput Phys*. 2000;161(1):35–60.
37. Uhlmann M. An immersed boundary method with direct forcing for the simulation of particulate flows. *J Comput Phys*. 2005;209(2):448–476.
38. Luo K, Wang Z, Fan J, Cen K. Full-scale solutions to particle-laden flows: multidirect forcing and immersed boundary method. *Phys Rev E*. 2007;76(9):066709.
39. Wang Z, Fan J, Luo K. Combined multi-direct forcing and immersed boundary method for simulating flows with moving particles. *Int J Multiphase Flow*. 2008;34(3):283–302.
40. Kriebitzsch SHL. Direct numerical simulation of dense gas-solid flows. Ph.D. Thesis. Eindhoven, The Netherlands: Eindhoven University of Technology, 2011.
41. Yu Z, Shao X. A direct-forcing fictitious domain method for particulate flows. *J Comput Phys*. 2007;227(1):292–314.
42. Breugem WP. A second-order accurate immersed boundary method for fully resolved simulations of particle-laden flows. *J Comput Phys*. 2012;231(13):4469–4498.
43. Kempe T, Fröhlich J. An improved immersed boundary method with direct forcing for the simulation of particle laden flows. *J Comput Phys*. 2012;231(9):3663–3684.
44. Tang Y, Kriebitzsch SHL, Peters EAJF, van der Hoef MA, Kuipers JAM. A methodology for highly accurate results of direct numerical simulations: drag force in dense gas-solid flows at intermediate Reynolds number. *Int J Multiphase Flow*. 2014;62:73–86.
45. Garg R, Tenneti S, Mohd-Yusof J, Subramaniam S. Direct numerical simulation of gas-solids flow based on the immersed boundary method. In: Pannala S, Syamlal M, O'Brien TJ, editors. *Computational Gas-Solids Flows and Reacting Systems: Theory, Methods and Practice*. Hershey, PA: IGI Global, 2011:245–276.
46. Felice RD. The voidage function for fluid-particle interaction systems. *Int J Multiphase Flow*. 1994;20(1):153–159.
47. Benyahia S, Syamlal M, O'Brien TJ. Evaluation of boundary conditions used to model dilute, turbulent gas/solids flows in a pipe. *Powder Technol*. 2005;156(2–3):62–72.
48. Schiller L, Naumann A. A drag coefficient correlation. *VDI Zeitung*. 1935;77:318–320.
49. Hoomans BPB, Kuipers JAM, Briels WJ, van Swaaij WPM. Discrete particle simulation of bubble and slug formation in a two-dimensional gas-fluidised bed: a hard-sphere approach. *Chem Eng Sci*. 1996;51(1):99–118.
50. Deen NG, van Sint Annaland M, Kuipers JAM. Multi-scale modeling of dispersed gas-liquid two-phase flow. *Chem Eng Sci*. 2004; 59(8–9):1853–1861.
51. Griffith BE, Peskin CS. On the order of accuracy of the immersed boundary method: higher order convergence rates for sufficiently smooth problems. *J Comput Phys*. 2005;208(1):75–105.
52. Frenkel D, Smit B. *Understanding Molecular Dynamics: From Algorithms to Applications*, 2nd ed., San Diego: Academic Press, 2001.
53. Noya EG, Vega C, de Miguel E. Determination of the melting point of hard spheres from direct coexistence simulation methods. *J Chem Phys*. 2008;128(15):154507.
54. Kumar N, Imole OI, Magnanimo V, Luding S. Deformation modes for assemblies of frictionless polydisperse spheres. *Adv Mat Research*. 2012;508:160–165.
55. Wylie JJ, Koch DL, Ladd AJC. Rheology of suspensions with high particle inertia and moderate fluid inertia. *J Fluid Mech*. 2003; 480(10):95–118.
56. Kriebitzsch SHL, van der Hoef MA, Kuipers JAM. Fully resolved simulation of a gas-fluidized bed: a critical test of DEM models. *Chem Eng Sci*. 2013;91:1–4.

Manuscript received May 14, 2014, and revision received Aug. 19, 2014.